

# Generalisable and distinctive 3D local deep descriptors for point cloud registration

Fabio Poiesi and Davide Boscaini

**Abstract**—An effective 3D descriptor should be invariant to different geometric transformations, such as scale and rotation, repeatable in the case of occlusions and clutter, and generalisable in different contexts when data is captured with different sensors. We present a simple but yet effective method to learn generalisable and distinctive 3D local descriptors that can be used to register point clouds captured in different contexts with different sensors. Point cloud patches are extracted, canonicalised with respect to their local reference frame, and encoded into scale and rotation-invariant compact descriptors by a point permutation-invariant deep neural network. Our descriptors can effectively generalise across sensor modalities from locally and randomly sampled points. We evaluate and compare our descriptors with alternative handcrafted and deep learning-based descriptors on several indoor and outdoor datasets reconstructed using both RGBD sensors and laser scanners. Our descriptors outperform most recent descriptors by a large margin in terms of generalisation, and become the state of the art also in benchmarks where training and testing are performed in the same scenarios.

**Index Terms**—Point cloud registration, deep learning-based descriptors, local reference frame, contrastive learning.

## 1 INTRODUCTION

3D point set registration is the problem of finding an optimal Euclidean transformation to align two overlapping 3D point sets such that they can be represented in a common reference frame. 3D point set registration is important for numerous applications including 3D reconstruction [1], relocalisation [2], and object 6D pose estimation [3]. 3D point set registration methods can estimate this transformation from the 3D points directly or from descriptors that are constructed based on their geometric information [4]–[10]. In particular, there exists two main methods. Methods that iteratively minimise the distance between nearest-neighbouring points if the initial reference frames of the point sets are (loosely) aligned, e.g. Iterative Closest Point (ICP) [11], and methods that find corresponding points through robust descriptor matching, e.g. using RANSAC [12], to compute the Euclidean transformation. In this paper we focus on the second problem, that is designing generalisable and distinctive compact descriptors for 3D point clouds that are captured in real-world scenarios [4]–[10]. This problem is particularly challenging because point clouds can be captured with different sensors (e.g. RGBD [5], LIDAR [13]) and in different contexts (e.g. indoors, outdoors), thus requiring descriptors to be equally effective across different scenarios.

Descriptors can be computed using one-stage [4]–[8] or two-stage [14]–[16] methods. The former produces descriptors by directly encoding the geometric information from raw points (e.g. coordinates, normals). The latter firstly transforms points into suitable representations (e.g. projection on another space [10], [17] or rigid transformation [9]), then encodes these new representations into descrip-

tors. Descriptors can in turn be handcrafted or based on deep learning. Deep learning-based descriptors [5]–[10], [16], [18]–[20] largely outperform their handcrafted counterpart [4], [14], [15], [21], [22]. The availability of GPU processing recently led to the formulation of deep learning-based methods that can produce per-point descriptors by processing entire point clouds rather efficiently [6]–[8], in a split second when sparse convolutions are used [7]. We refer to these descriptors as global descriptors because they encode the global context. Although global descriptors can be computed efficiently, they lack generalisation ability when trained with data captured in a context and used in other contexts [9], [10]. Differently, descriptors that encode local geometric information have a greater generalisation ability, although being computationally less efficient than their global counterpart [9], [10], [16].

In this paper we present a novel deep learning-based two-stage method to compute Generalisable and Distinctive (GeDi) local descriptors for point cloud registration. Given a patch defined as a set of neighbouring points, we achieve rotation-invariance by computing a local reference frame (LRF) that aims to rigidly transform the patch into its canonical representation [22]. We process this canonicalised patch using a point permutation-invariant deep neural network to produce the unitary-length descriptor of the patch [23]. Our deep network uses receptive fields with different sizes to encode and aggregate local geometric information at multiple scales. To mitigate the problem of an incorrectly estimated LRF, we learn a quaternion transformation network (QNet) that refines the canonicalisation operation before encoding the points into a descriptor. We train QNet and the encoding network concurrently using contrastive learning [7] with a Siamese approach. Our contrastive learning mines for quadruplets and induces corresponding patches extracted from two different and overlapping point clouds to have descriptors as similar as possible, while explicitly making non-corresponding patches to be as dissimilar as

- *Fabio Poiesi and Davide Boscaini are with the Technologies of Vision Lab in Fondazione Bruno Kessler, Trento, Italy. E-mails: poiesi@fbk.eu, dboscaini@fbk.eu.*
- *This research was partially supported by Provincia Autonoma di Trento (Italy) under L.P. 6/99 as part of the X-Loader4.0 project.*

*Manuscript received mm dd, yyyy; revised mm dd, yyyy.*

possible. We perform an extensive evaluation by assessing the generalisability and distinctiveness of GeDi descriptors on three large-scale datasets, i.e. ETH [24], KITTI [13] and 3DMatch [5]. We compare our method with 18 methods from the literature and show that GeDi outperforms the most recent methods in terms of generalisability by a large margin, while also being as effective as the other descriptors when trained and tested in the same scenarios. The source code will be made publicly available at <https://github.com/fabiopoiesi/gedi>.

This paper extends our earlier work [9] in many aspects. We modify the deep neural network architecture used in [9] in order to process patches at multiple scales. We introduce QNet to effectively achieve multi-scale processing, which brings two main benefits. Firstly, QNet ensures that the transformation applied to the canonicalised points is  $SO(3)$ , property that is not guaranteed with the spatial transformer network (TNet) used in [9]. By construction, TNet produces a transformation that could be different from  $SO(3)$ . Therefore, TNet may distort the canonicalised points, thus making multi-scale processing and aggregation inconsistent across neighbourhoods with different sizes. These unpredictable variations can lead to convergence problems in training. Secondly, QNet can be trained effectively without needing the dedicated Chamfer loss [20] for TNet that we used in [9]. Inspired by [25], we change our training strategy, moving from a farthest-point-sampling strategy for sampling patches from point cloud pairs to a fully randomised strategy. In [9], we processed the same points during training because we relied on data pre-processing as in [16]. In this new work we perform random sampling at each iteration for the points transformed with the LRF and also for the canonicalised points consumed by the deep network. This fully randomised approach enables us to make training more efficient, thus allowing training to be carried out with larger minibatches and with an improved diversity in the processed data. We also provide a more comprehensive review of related works. Lastly, we significantly expand our experimental evaluation and analysis, considering more recent methods, adding a new dataset (i.e. KITTI [13]), and showing additional qualitative and quantitative results.

The remainder of this paper is organised as follows. Sec 2 reviews the related work. Sec. 3 describes our approach. Sec. 4 reports our quantitative and qualitative experiments, and assesses our implementation choices via ablation study. Sec. 5 draws the conclusions.

## 2 RELATED WORK

Descriptors for point cloud registration can be designed using handcrafted or deep learning-based algorithms, which in turn can be computed using one-stage or two-stage methods. Typically, handcrafted methods use histograms to encode local geometric structures, such as point coordinates, surface normals, and/or pairwise point/normal relationships, whereas deep learning-based methods use deep networks to learn representations from either global or local geometric structures. Regardless their formulation, all these descriptors can be used together with point cloud registration algorithms, for example using fast global registration [26] or based on RANSAC [12].

*Handcrafted one-stage methods* aim to compute point representations that can enable descriptors to be repeatable and robust to different transformations (e.g. scale, rotation). Typically, these methods compute descriptors from point representations that are defined between pairs of points using 3D point coordinates only [27] and/or also surface normals [3], [4], [14]. The former includes the MCOV descriptor that is based on the computation of a covariance matrix encoding the correlation between the geometric and the photometric information extracted from a point cloud patch [27], such as the angle between points and the RGB value of each point. This covariance matrix is then directly used as the patch descriptor. The authors of MCOV show that local representations promote robustness to rigid spatial transformations, clutter and variations of point density. The latter includes descriptors such as Spin-image [14], Fast Point Feature Histograms (FPFH) [4] and Point-Pair Features (PPF) [3]. The Spin-image descriptor is based on rotation-invariant parametric representations of the points belonging to the patch relative to the coordinate and the normal of its centroid [14]. These representations are projected on 2D image planes and turned into a descriptor by computing the image histogram. Similarly to Spin-image, FPFH and PPF use features that are computed as distances and relative angles between points and normals. Unlike Spin-image, FPFH descriptors are defined as histograms of these features directly. Differently, PPF is used to build a representation of a point cloud in the form of hash table in order to make the task of point cloud registration efficient. While FPFH can be used to register large point clouds, PPF is more suitable for object 6D pose estimation problems, i.e. find the pose of small objects within larger point clouds.

*Handcrafted two-stage methods* aim to compute descriptors by decomposing the computation of the descriptor into the estimation of a local reference frame (LRF), typically computed using points belonging to the patch, and the formulation of a compact representation that encodes the geometric properties of these points represented with respect to their LRF. This category includes the Intrinsic Shape Signatures (ISS) descriptor that use the eigenvalue decomposition of a weighted covariance matrix to estimate the LRF [21]. The covariance matrix is obtained by aggregating the contribution of points in the neighbourhood of the patch centroid. The weights penalise distant points from the centroid. The ISS descriptor is built using the occupational histogram of a spherical neighbourhood with a predefined radius around the centroid. Similarly to ISS, the Signature of Histograms of Orientations (SHOT) descriptor computes the LRF through the eigenvalue decomposition of the covariance matrix to find two orthogonal axes [15]. Unlike ISS, SHOT employs an ad-hoc strategy to disambiguate the sign of these axes based on the geometric structure of the points belonging to the patch. The third axis is the result of the cross product between the other two axes. SHOT computes the descriptor as a combination of the occupational histogram and of the geometric properties of the points relative to the centroid of the patch. To produce a LRF with higher robustness to clutter, the Triple Orthogonal Local Depth Images (TOLDI) descriptor extends SHOT by introducing a weighted aggregation of the points [22]. TOLDI is then constructed by building image histograms from the result of the projections

of the points on the three planes defined by the LRF axes. Unlike, ISS, SHOT and TOLDI, the Rotational Projection Statistics (RoPS) [28] descriptor is computed by projecting the points transformed by its LRF onto 2D planes and by calculating a set of geometric statistics, such as low-order central moments and entropy, from the distributions of these projected points. RoPS' LRF uses the local point connectivity information to calculate the eigenvalue decomposition on the scatter matrix.

*Deep learning-based one-stage methods* aim to compute descriptors by training deep neural networks to process input points and/or features calculated from geometric relationships between pairs of points. This category includes the 3DMatch approach where point cloud patches are transformed into volumetric voxel grids of Truncated Distance Function values and given as input to a 3D convolutional neural network to output local descriptors [5]. In addition to using point coordinates, the PPFNet approach also provides normals and PPF representations [3] of the points within the patch as input to a PointNet-based deep network [29]. This deep network aggregates local and global features to build global descriptors [6]. Unlike PPFNet, PPF-FoldNet discards the point coordinate and normal information, and learns to produce global descriptors from the PPF representations directly [18]. PPF-FoldNet implements the idea of learning descriptors using an end-to-end autoencoder [30] that is trained to reconstruct the input, i.e. PPF representations. Like PPFNet, PPF-FoldNet uses a PointNet-based deep neural network [29]. The FCGF approach uses a fully-convolutional deep network to generate global descriptors thought 3D sparse convolutions [7], [31]. FCGF can process the complete point cloud and outputs a descriptor for each point. Although the complete point cloud is processed, these sparse convolutions allow FCGF to be rather computationally efficient. Similarly to FCGC, the D3Feat approach uses a fully convolutional network [8], but unlike FCGC, D3Feat extracts global descriptors using dense deep features through a KPConv backbone [32].

*Deep learning-based two-stage methods* aim to compute descriptors by training deep neural networks to process input points that are either canonicalised with respect to their LRF or projected to some parametric spaces. The 3DSmoothNet approach uses the TOLDI approach to estimate the LRF of a patch and applies it to the points before processing them with a deep neural network [16], [22]. As 3DMatch, 3DSmoothNet builds volumetric voxel grids in order to process them with a 3D convolution neural network, however instead of assigning Truncated Distance Function values to the voxels, 3DSmoothNet computes Gaussian smoothed representations based on the coordinates of the points within the patch. As 3DSmoothNet, the distinctive local 3D descriptors (DIP) use the TOLDI approach to canonicalise points [9]. These are then given as input to a PointNet-based deep network to produce local descriptors. DIP uses a transformation network on the input points to improve eventual noisy canonicalisations. Unlike 3DSmoothNet and DIP, the local multi-view descriptors (LMVD) performs multi-view image rendering with a differentiable renderer of the points of a patch [17]. LMVD produces local descriptors by extracting localised features maps from each view and by fusing them via a soft-view pooling module. The SpinNet

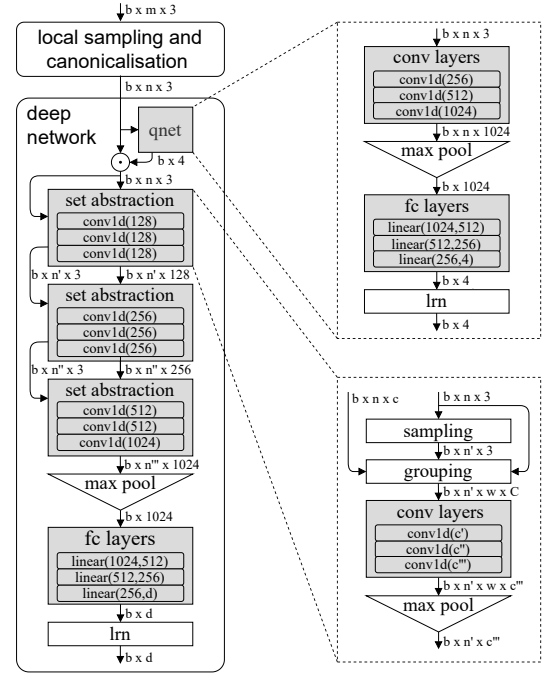


Fig. 1. Block diagram of our approach to compute GeDi descriptors given a set of  $b$  input patches, each one composed of  $m$  3D points. The first stage involves the computation of the local reference frames, the canonicalisation of each patch and the subsampling of each patch to  $n$  points. The second stage involves the computation of a descriptor for each subsampled canonicalised patch through a deep network with permutation invariant properties on the  $n$  input points. The quaternion network (qnet) outputs a quaternion for each patch whose  $SO(3)$  transformation is applied to the  $n$  points through the  $\odot$  operator before processing them through a series of set abstraction layers. Each set abstraction layer involves *sampling* to randomly select a set of centroids equidistant from each other, *grouping* to aggregate the nearest neighbouring points of these centroids, encoding to lift the dimensionality of each point through a series of *convolutional layers* and *max pooling* to build a high-dimensional representation for each centroid. After the third set abstraction layer, the max pooling operation outputs a 1024-dimensional representation for each patch that is processed through a multilayer perceptron (mlp). The mlp outputs a  $d$  dimensional representation that is normalised by a local response normalisation (lrm) layer.

approach uses a spatial point transformer to project the input point to a cylindrical space in order to produce rotation invariant representations [10]. A deep network based on 3D cylindrical convolutional layers is then employed to output local descriptors.

### 3 OUR APPROACH

Let  $\mathcal{X} = \{\mathbf{x}\} \subset \mathcal{P}$  be a local patch extracted from a point cloud  $\mathcal{P} \subset \mathbb{R}^3$ , where  $\mathcal{X}$  is an unordered set of 3D points. We design an algorithm that calculates a compact descriptor of  $\mathcal{X}$  such that  $\mathbf{f} = (\Phi_{\Theta} \circ \Psi)(\mathcal{X})$ , where  $\mathbf{f} \in \mathbb{R}^d$  is the  $d$ -dimensional descriptor of  $\mathcal{X}$ ,  $\Psi$  is the function that samples and canonicalises the points of  $\mathcal{X}$  through the computation of the local reference frame, and  $\Phi_{\Theta}$  is a deep neural network with learnable parameters  $\Theta$ . Without loss of generality we use the 3D coordinates of the points to compute  $\mathbf{f}$ , i.e.  $\mathbf{x} = (x, y, z)$ . Fig. 1 shows the block diagram of our method to compute  $\mathbf{f}$  given  $\mathcal{X}$ .

### 3.1 Local sampling and canonicalisation

Local sampling and canonicalisation involves a sequence of operations that include: (i) patch extraction, (ii) estimation of the local reference frame, and (iii) point sampling to prepare the points to be processed by the deep network.

#### 3.1.1 Patch extraction

We define a patch centred in  $\hat{\mathbf{x}} \in \mathcal{P}$  as  $\mathcal{X} = \{\mathbf{x} : \|\mathbf{x} - \hat{\mathbf{x}}\|_2 \leq r\}$ , where  $\|\cdot\|_2$  denotes the Euclidean norm and  $r$  is the radius of the patch. Patches extracted from different regions of  $\mathcal{P}$  may have different cardinalities due to, e.g., occlusions or clutter. In order to learn a general representation for patches that include same geometric structures but with different cardinalities, we randomly sample  $m$  points within  $\mathcal{X}$ . In the case of patches with less than  $m$  points, we use padding by randomly picking points within  $\mathcal{X}$  until  $m$  points are sampled. Moreover, patches with the same cardinality allow us to efficiently train  $\Phi_{\Theta}$  using batch processing. Let  $S_m$  be the sampling function to produce the set of randomly sampled points  $\tilde{\mathcal{X}} = S_m(\mathcal{X})$ , where  $\tilde{\mathcal{X}} \subset \mathcal{X}$  and  $|\tilde{\mathcal{X}}| = m$ .

#### 3.1.2 Local reference frame estimation

The local reference frame (LRF) estimation of  $\hat{\mathbf{x}}$  involves the computation of three orthogonal axes: an axis corresponding to the normal of a plane tangent to  $\mathcal{X}$  in  $\hat{\mathbf{x}}$ , an axis corresponding to a repeatable vector lying on this plane, and an axis that is orthogonal to the previous two axes [22].

Let  $\Sigma_{\tilde{\mathcal{X}}}$  be the covariance matrix of the patch  $\tilde{\mathcal{X}}$  computed with respect to its centre  $\hat{\mathbf{x}}$ , i.e.

$$\Sigma_{\tilde{\mathcal{X}}} = \frac{1}{m} \sum_{\mathbf{x} \in \tilde{\mathcal{X}}} (\mathbf{x} - \hat{\mathbf{x}})(\mathbf{x} - \hat{\mathbf{x}})^\top, \quad (1)$$

where  $\cdot^\top$  is the transpose operator. The normal of  $\hat{\mathbf{x}}$  can be defined as the smallest eigenvector  $\mathbf{e}_{\hat{\mathbf{x}}}$  of  $\Sigma_{\tilde{\mathcal{X}}}$ . To cope with the sign ambiguity resulting from the eigendecomposition, we define

$$\mathbf{w}_{\hat{\mathbf{x}}} = \begin{cases} \mathbf{e}_{\hat{\mathbf{x}}}, & \text{if } \sum_{\mathbf{x} \in \tilde{\mathcal{X}}} \mathbf{e}_{\hat{\mathbf{x}}} \cdot (\hat{\mathbf{x}} - \mathbf{x}) \geq 0 \\ -\mathbf{e}_{\hat{\mathbf{x}}}, & \text{otherwise} \end{cases}, \quad (2)$$

where  $\cdot$  is the dot product [15].

Let  $\Pi_{\hat{\mathbf{x}}}$  be the plane with normal  $\mathbf{w}_{\hat{\mathbf{x}}}$  and tangent to  $\tilde{\mathcal{X}}$  in  $\hat{\mathbf{x}}$ . The computation of the vector lying on  $\Pi_{\hat{\mathbf{x}}}$  should ideally be repeatable across all the patches including the same geometric structure. However, noise, such as occlusion or clutter, makes repeatability challenging to achieve. As in [22], we compute this vector as a linear combination of the vectors pointing from the centre of the patch, i.e.  $\hat{\mathbf{x}}$ , to the other points in the patch  $\mathbf{x} \in \tilde{\mathcal{X}}$ . The multipliers of the linear combination weigh (i) the distances from the centre to the points of the patch, and (ii) the distances from the centre to the projections of the points on  $\Pi_{\hat{\mathbf{x}}}$ . Let  $\mathbf{u}_{\hat{\mathbf{x}}}$  be the vector lying on  $\Pi_{\hat{\mathbf{x}}}$  such that  $\mathbf{w}_{\hat{\mathbf{x}}} \cdot \mathbf{u}_{\hat{\mathbf{x}}} = 0$ . We compute  $\mathbf{u}_{\hat{\mathbf{x}}}$  as

$$\mathbf{u}_{\hat{\mathbf{x}}} = \frac{1}{\|\sum_{\mathbf{x} \in \tilde{\mathcal{X}}} \alpha_{\hat{\mathbf{x}}} \beta_{\hat{\mathbf{x}}} \nu_{\hat{\mathbf{x}}}\|_2} \sum_{\mathbf{x} \in \tilde{\mathcal{X}}} \alpha_{\hat{\mathbf{x}}} \beta_{\hat{\mathbf{x}}} \nu_{\hat{\mathbf{x}}}, \quad (3)$$

where  $\alpha_{\hat{\mathbf{x}}}$  and  $\beta_{\hat{\mathbf{x}}}$  are the weights that are computed as

$$\alpha_{\hat{\mathbf{x}}} = (r - \|\mathbf{x} - \hat{\mathbf{x}}\|_2)^2 \quad (4)$$

and

$$\beta_{\hat{\mathbf{x}}} = ((\mathbf{x} - \hat{\mathbf{x}}) \cdot \mathbf{w}_{\hat{\mathbf{x}}})^2, \quad (5)$$

while  $\nu_{\hat{\mathbf{x}}}$  is the projection of the vector  $(\mathbf{x} - \hat{\mathbf{x}})$  on  $\Pi_{\hat{\mathbf{x}}}$ , i.e.

$$\nu_{\hat{\mathbf{x}}} = (\mathbf{x} - \hat{\mathbf{x}}) - ((\mathbf{x} - \hat{\mathbf{x}}) \cdot \mathbf{w}_{\hat{\mathbf{x}}}) \mathbf{w}_{\hat{\mathbf{x}}}. \quad (6)$$

The third axis is computed as  $\mathbf{v}_{\hat{\mathbf{x}}} = \mathbf{w}_{\hat{\mathbf{x}}} \times \mathbf{u}_{\hat{\mathbf{x}}}$ , where  $\times$  is the cross product. We combine these three axes into a rotation matrix that we use to canonicalise the points in  $\tilde{\mathcal{X}}$ . Let  $\mathbf{R}_{\hat{\mathbf{x}}} = [\mathbf{u}_{\hat{\mathbf{x}}}, \mathbf{v}_{\hat{\mathbf{x}}}, \mathbf{w}_{\hat{\mathbf{x}}}]^\top$  be the rotation matrix for the patch  $\tilde{\mathcal{X}}$  centred in  $\hat{\mathbf{x}}$  that transforms  $\tilde{\mathcal{X}}$  from the global reference frame of  $\mathcal{P}$  to the LRF.

#### 3.1.3 Re-sampling and normalisations

Before transforming the points of the patch with respect to their LRF, we sample  $n$  points from  $\tilde{\mathcal{X}}$ , where  $n < m$ . Let  $S_n$  be the sampling function to produce the set of randomly sampled points  $\tilde{\mathcal{X}} = S_n(\tilde{\mathcal{X}})$ , where  $\tilde{\mathcal{X}} \subset \tilde{\mathcal{X}}$  and  $|\tilde{\mathcal{X}}| = n$ . To promote descriptor translation invariance, we represent the coordinates of  $\tilde{\mathcal{X}}$  relative to their patch centre  $\hat{\mathbf{x}}$ . To promote descriptor scale invariance, we normalise these relative coordinates by the radius of the patch  $r$ ,

$$\Psi(\tilde{\mathcal{X}}) = \{\mathbf{y} : \mathbf{y} = \mathbf{R}_{\hat{\mathbf{x}}}((\mathbf{x} - \hat{\mathbf{x}})/r), \mathbf{x} \in S_n(\tilde{\mathcal{X}})\}, \quad (7)$$

which becomes the input to our deep network.

Here we sample fewer points than in Sec. 3.1.1 to speed up the deep network computation, to handle large batches during training and because we experimentally observed that distinctiveness performance is upper-bounded when a certain number of points is reached.

## 3.2 Deep network design

Because  $\Psi(\tilde{\mathcal{X}})$  generates an unordered set of points, we use a deep network that is robust to permutations of the input points [23], [33]. Unlike DIP descriptors [9], which are computed using a single receptive field for the whole set of input points [29], our deep network uses a hierarchical structure of the receptive fields to build high-dimensional representations from local geometric structures at multiple scales [23]. In particular, our deep network learns to aggregate and to encode these representations using different kernel sizes along the hierarchy, making our descriptors more generalisable and distinctive than DIP. However, because these multi-scale receptive fields cannot be used along with the spatial transformer network used in DIP, we design a different spatial transformer network that, instead of producing a  $3 \times 3$  transformation, outputs a quaternion.

#### 3.2.1 Backbone

To aggregate and encode local geometric representations for each patch, we use a PointNet++ deep network [23]. PointNet++ applies PointNet recursively on nested neighbourhoods of the input set, promoting robustness to noise and allowing our descriptors to encode richer geometric structures. PointNet++ is designed as a sequence of set abstraction layers (Fig. 1). Each abstraction layer lifts point representation to a higher dimensional embedding space by aggregating local geometric structures. These representations are propagated to the next layers where representations of spatially close points at larger scales are further aggregated

in higher dimensional representations. Each set abstraction layer is composed of three layers, i.e. the *sampling layer*, the *grouping layer* and the *representation layer*. The *sampling layer* operates in the metric space and produces a subset of the input centroids using the Farthest Point Sampling (FPS) algorithm [23]. For each centroid, the *grouping layer* aggregates spatially neighbouring points. This operations consists of a neighbour search using a spherical kernel with fixed radius and centred on the centroid. A subset of the points within this sphere are selected to be processed by the *representation layer*, which uses a PointNet-like architecture to produce high-dimensional representations of the aggregated points. The output of the last set abstraction layers is fed to a max pooling layer that reduces the last representations to a 1024-dimensional representation vector. This representation vector is processed through a multilayer perceptron to produce a  $d$ -dimensional vector. Lastly, we use a Local Response Normalisation (LRN) layer to transform this vector into a descriptor  $\mathbf{f}$  with unitary norm. LRN consists of a L2 normalisation of the last multilayer perceptron’s  $d$ -dimensional output. We found that LRN improves training stability and convergence [7], [16], [34].

### 3.2.2 Quaternion network

The LRF estimation may be noisy due to clutter or occlusions. A deep network that corrects noisy transformations can promote descriptor repeatability. In our previous work [9] we used the spatial transformer network proposed in PointNet, namely TNet [29], to estimate a transformation that can correct eventual noisy canonicalisations when it is applied to the input points. We found this solution to be unsuitable for the current backbone because the transformation learned by a TNet is not constrained to be  $SO(3)$ , i.e. the input points can undergo scale and skew transformations. Since the grouping layer operates in the metric space using a fixed radius (Sec. 3.2.1), the neighbourhood search would select points inconsistently across different patches. This behaviour may undermine repeatability and generalisation. To mitigate this problem, Qi et al. [29] propose to constrain TNet’s output to be  $SO(3)$  via the loss regularisation term  $\ell_{\text{reg}} = \|\mathbf{I} - \mathbf{A}\mathbf{A}^T\|_F^2$ , where  $\mathbf{A} \in \mathbb{R}^{3 \times 3}$  is TNet’s output. This solution did not work in our experiments, the  $\ell_{\text{reg}}$  term made our loss diverge. Therefore, inspired by [35], we designed a deep network that outputs a unit-norm quaternion, which is a  $SO(3)$  transformation by construction. We name this deep network QNet. Similarly to TNet, QNet is based on PointNet [29] (Fig. 1). We add a local responses normalisation layer to the output of PoinNet in order to produce the desired vector with unit norm. We experimentally observed that QNet can be learned concurrently with our backbone, without the need of an additional alignment loss, like the Chamfer loss used in DIP [9].

### 3.2.3 Training procedure

Our ultimate goal is to produce descriptors that are as similar as possible amongst corresponding patches of different point clouds, and that are as dissimilar as possible amongst non-corresponding patches. Therefore, we set the objective of our training to produce descriptors whose distance is minimised for corresponding patches of pairs of overlapping point clouds. We train our network following

a Siamese approach that processes pairs of corresponding patches using two branches with shared weights [6], [16]. Fig. 2 illustrates our training procedure.

We begin the training procedure by selecting point clouds that have an overlap region of at least  $\tau_o$  [8], [10], [16]. We randomly sample  $b$  pairs of corresponding points from this overlap region, which we treat as our patch centres. We perform local sampling and canonicalisation for each patch (Sec. 3.1), and we give the result of this operation as input to our Siamese deep networks with shared parameters. Each branch independently calculates a descriptor for a given patch. We learn these parameters by minimising a contrastive loss through the mining of the hardest negative samples within a minibatch [7]. Given a pair of anchor descriptors  $(\mathbf{f}, \mathbf{f}')$ , we mine the hardest negatives  $(\tilde{\mathbf{f}}, \tilde{\mathbf{f}}')$  and define the loss as

$$\ell = \frac{1}{b} \sum_{(\mathbf{f}, \mathbf{f}') \in \mathcal{C}_+} \left( \frac{1}{|\mathcal{C}_+|} [d(\mathbf{f}, \mathbf{f}') - m_+]_+^2 + \frac{1}{2|\mathcal{C}_-(\mathbf{f})|} [m_- - \min_{\tilde{\mathbf{f}} \in \mathcal{C}_-(\mathbf{f})} d(\mathbf{f}, \tilde{\mathbf{f}})]_+^2 + \frac{1}{2|\mathcal{C}_-(\mathbf{f}')|} [m_- - \min_{\tilde{\mathbf{f}}' \in \mathcal{C}_-(\mathbf{f}')} d(\mathbf{f}', \tilde{\mathbf{f}}')]_+^2 \right), \quad (8)$$

where  $\mathcal{C}_+$  is the set of the anchor pairs,  $\mathcal{C}_-$  is the set of descriptors created from the randomly sampled patches,  $m_+$  and  $m_-$  are the margins for anchor and negative pairs, respectively, and  $[\cdot]_+$  takes the positive part of its argument. There exist several techniques to mine negatives. In our previous work [9] we used a FPS-based approach in order to avoid selecting negatives that are spatially close to the anchors. Instead, in Eq. 8 we mine negatives outside a spherical region of radius  $r_C$  centred on each anchor [7]. We experimentally found that random sampling of patches combined with the safe boundaries of the spherical regions around the anchors can be implemented efficiently. This enables us to build larger mini-batches and to introduce more randomness in the training process. Similar benefit from the randomisation process as opposed to farthest point sampling have also been experienced for point cloud segmentation tasks in [25]. We define  $\mathcal{C}_-$  as

$$\mathcal{C}_-(\mathbf{f}) = \{\tilde{\mathbf{f}} : \|\tilde{\mathbf{x}} - \hat{\mathbf{x}}\|_2 > r_C, \tilde{\mathbf{f}} \in \mathcal{C}_-\}. \quad (9)$$

The hardest-contrastive loss allows the deep network to learn informative descriptors that effectively capture local geometric structures. Fig. 3 shows the principal components of our descriptors on point cloud examples extracted from 3DMatch [5], ETH [24] and KITTI [13] datasets. We use Principal Component Analysis to obtain the principal components [36]. For each point, we map the three most representative principal components of their descriptor in RGB. Each point cloud is processed independently, therefore colours across examples are not necessary related with each other. From these examples we can observe that descriptors of similar geometric structures are consistently clustered in their colour space as their principal components are similar. Flat surfaces, e.g. roads and floors, or vegetation are mapped with the same colours. In a) we can observe that different parts of the sofa are clustered together, e.g. corners and

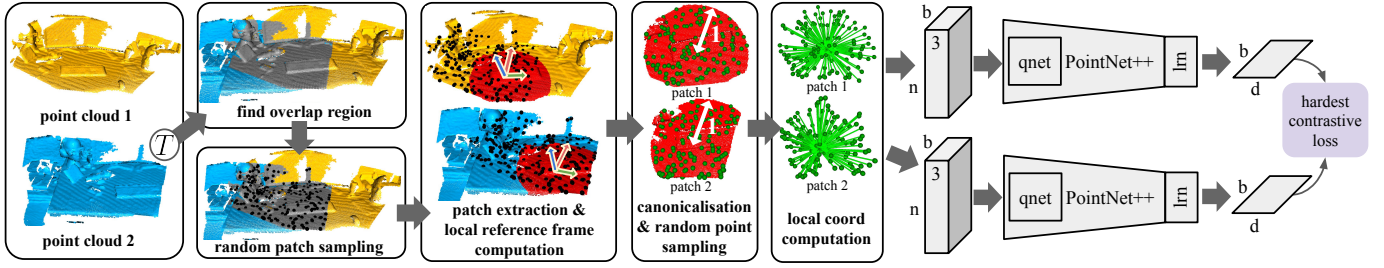


Fig. 2. GeDi’s training pipeline. Two overlapping point clouds are aligned using the ground-truth transformation ( $T$ ). From the overlap region (grey), we randomly sample  $b$  points (black) and use them as patch centres. We use a Siamese approach to train two deep neural networks with shared parameters concurrently. For deep network, we perform the following operations: (i) for each centre (black) a patch (red) with radius  $r$  is extracted and the corresponding local reference frame is computed using the points of the patch [16]; (ii) this patch is canonicalised using the local reference frame and  $n$  points are randomly sampled from the patch (green points); (iii) the coordinates of these  $n$  points are represented relative to the patch centre and normalised to obtain patches with unitary radius; (iv) these  $n$  points are given to the deep networks as input to learn the descriptor. The local response normalisation (lrrn) layer outputs descriptors with unitary norm. We train the deep network using the hardest-contrastive loss [7].

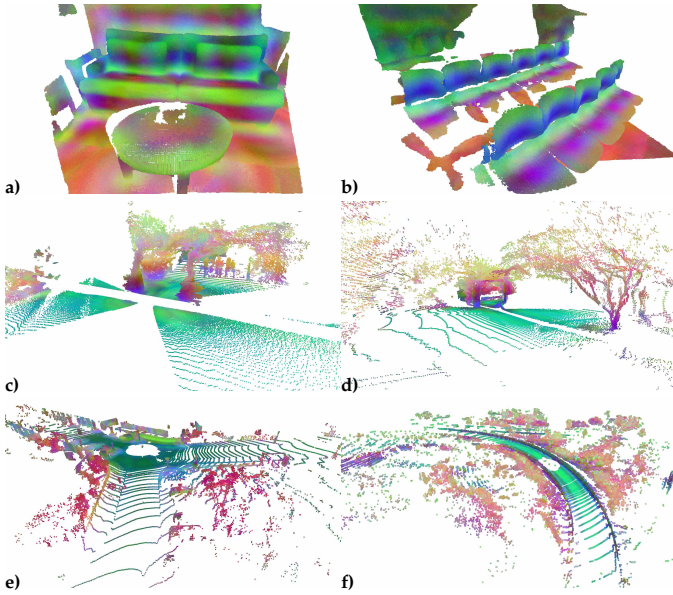


Fig. 3. Colour-coded principal components of our descriptors on point clouds extracted from (a,b) 3DMatch [5], (c,d) ETH [24] and (e,f) KITTI [13] datasets. We use Principal Component Analysis [36] to extract the principal components. For each point, we map the three most representative principal components of their descriptor in RGB. Each point cloud is processed independently, therefore colours across examples may not necessarily be related with each other. From these examples we can observe that descriptors of similar geometric structures are consistently clustered in their colour space as their principal components are similar.

centres of the cushions. In b), although some chair parts of the back row, i.e. seats, are incomplete due to occlusions occurred during the acquisition of the point cloud, we can observe that they are consistently clustered in the same colour space as those of the front row.

## 4 EXPERIMENTS

We evaluate the generalisation ability of GeDi descriptors using large-scale point cloud datasets that have been captured with different sensors (e.g. Kinect, LIDAR) in different contexts (indoors, outdoors). We evaluate and compare GeDi with other descriptors using the same datasets and evaluation measures that are used in the literature [7], [8], [10], [16]. Most of the descriptors used for comparison are

described in Sec. 2. Lastly, we perform an ablation study to analyse the effectiveness of GeDi’s architectural elements.

### 4.1 Datasets

We use three real-world large-scale datasets: 3DMatch [5], ETH [24], and KITTI [13]. For each dataset we use the same train/test splits used in literature [7], [8], [10].

The 3DMatch dataset is composed of 62 indoor scenes captured with different RGB-D sensors<sup>1</sup>, containing dense point clouds of reconstructed rooms with various appliances and furnitures. 3DMatch is a collection of datasets from different repositories including Analysis-by-Synthesis [37], 7-Scenes [38], SUN3D [39], RGB-D Scenes v.2 [40], and Halber and Funkhouser [41]. The train/test split is 54/8, where each scene includes partially overlapping and registered point cloud pairs. We use the point cloud pairs whose overlap is  $\tau_o \geq 30\%$ , resulting in about 16.6K pairs for training and about 1.66K pairs for testing [8], [10], [16]. We use the ground-truth transformations provided by Gojcic et al. [16]. To evaluate GeDi’s rotation invariance ability, we follow the evaluation of [8], [10], [16] and create an augmented version of 3DMatch, namely 3DMatchRotated, where each point cloud is rotated around all the three axes by angles uniformly and independently sampled in  $[0^\circ, 360^\circ]$ .

The ETH dataset contains four outdoor scenes captured with a laser scanner<sup>2</sup>. We use the following sequences: *Gazebo-Summer*, *Gazebo-Winter*, *Wood-Summer* and *Wood-Autumn*, which contain partially overlapping point clouds containing also vegetation [8], [10], [16]. These sequences are used only for testing and include 713 point cloud pairs. As in 3DMatch, we use the ground-truth transformations provided by Gojcic et al. [16].

The KITTI dataset contains 11 sequences of outdoor driving scenarios captured using a laser scanner<sup>3</sup>. The train/test split is 6/3, 0 to 5 for training and 8 to 10 for testing (6 and 7 are used for validation). The ground-truth transformations are measured by the odometry system of the vehicle recording the scenes. As in [7], [8], we use the Iterative

1. <https://3dmatch.cs.princeton.edu/>, last access: May 2021.  
 2. <https://projects.asl.ethz.ch/datasets/doku.php?id=laserregistration:laserregistration>, last access: May 2021.  
 3. [http://www.cvlibs.net/datasets/kitti/eval\\_odometry.php](http://www.cvlibs.net/datasets/kitti/eval_odometry.php), last access: May 2021.

Closest Point (ICP) algorithm to reduce noise in the ground-truth transformations. Only point cloud pairs that are 10m distant from each other are selected for training and testing, resulting in 1.4K pairs for training and 555 pairs for testing.

In our first experiment we train on the point clouds of 3DMatch and test on the (unseen) point clouds of ETH, KITTI [10]. In our second experiment we invert the train/test setup, i.e. we train on the point clouds of KITTI and test on the (unseen) point clouds of 3DMatch. In our last experiment we train and test on data of the same datasets according to their respective original train/test splits.

## 4.2 Evaluation measures

We evaluate the generalisation ability of GeDi by training and testing on different datasets. We use the feature-matching recall (FMR) metric to quantify the descriptor quality and to compare our results with those of alternative approaches in the case of 3DMatch and ETH [6]–[8], [10], [16], [42]. FMR is defined as

$$\Xi = \frac{1}{|\mathcal{F}|} \sum_{s=1}^{|\mathcal{F}|} \mathbb{1} \left( \underbrace{\left[ \frac{1}{|\Omega_s|} \sum_{(\mathbf{x}, \mathbf{x}') \in \Omega_s} \mathbb{1}(\|\mathbf{x} - \mathbf{T}_s \mathbf{x}'\|_2 < \tau_1) \right]}_{\xi_{\Omega_s}} > \tau_2 \right), \quad (10)$$

where  $|\mathcal{F}|$  is the number of matching point cloud pairs having  $\tau_o \geq 30\%$  (overlap between each other).  $(\mathbf{x}, \mathbf{x}')$  is a pair of corresponding points found in the descriptor space via a mutual nearest-neighbour search [16].  $\Omega_s$  is the set that contains all the found pairs  $(\mathbf{x}, \mathbf{x}')$  in the overlap regions  $\mathcal{O} \subset \mathcal{P}$  and  $\mathcal{O}' \subset \mathcal{P}'$ , respectively.  $\mathbf{T}_s$  is the ground-truth transformation alignment between  $\mathcal{P}'$  and  $\mathcal{P}$ .  $\mathbb{1}(\cdot)$  is the indicator function.  $\tau_1 = 10\text{cm}$  and  $\tau_2 = 0.05$  are set based on the theoretical analysis that RANSAC [12], [43] will find at least three corresponding points that can provide the correct  $\mathbf{T}_s$  with probability 99.9% using no more than  $\approx 55K$  iterations [6], [16]. In addition to  $\Xi$ , we also report mean ( $\mu_\xi$ ) and standard deviation ( $\sigma_\xi$ ) of  $\xi_{\Omega_s}$  before applying  $\tau_2$ .

In KITTI, we randomly select a set of points from each point cloud pair, compute their descriptors, and use RANSAC [12] through nearest neighbour search in the descriptor space to estimate the rigid transformation (rotation and translation) that aligns them to a common reference frame. We use the same configuration as [42]: we terminate RANSAC when the maximum number of iterations (10K) is reached or when the solution at 99% confidence is found. No further refinement is carried out, e.g. through ICP. The estimated rigid transformation is compared to the ground-truth transformation using the Relative Translational Error (RTE) and Relative Rotation Error (RRE) [44]. RTE is calculated as

$$RTE = \|\mathbf{T}_g - \mathbf{T}_e\|_2, \quad (11)$$

where  $\mathbf{T}_g$  is the ground-truth translation and  $\mathbf{T}_e$  is the estimated translation. RRE is calculated as

$$RRE = \sum_{i=0}^2 |a(\mathbf{R}_g^\top \mathbf{R}_e, i)|, \quad (12)$$

where  $\mathbf{R}_g$  is the ground-truth rotation,  $\mathbf{R}_e$  is the estimated rotation and  $a(\cdot, i)$  is the  $i^{\text{th}}$  Euler angle of the resulting rotation matrix. We compute the success rate by considering

the registration successful when the RTE and RRE are both below the thresholds 2m and  $5^\circ$ , respectively. We also report the average RTE and RRE values for the successful cases. Note that, as opposed to RTE and RRE, FMR does not require RANSAC as it directly averages the number of correctly matched point clouds across datasets.

## 4.3 Parameters

For training, we randomly sample  $b = 350$  patch centres in the overlap region between each point cloud pair. In 3DMatch we sample  $m = 4000$  points for the LRF computation, while we use  $m = 2000$  in the case of KITTI because its point clouds are sparser than those of 3DMatch. We experimentally observed that increasing  $m$  values have minor effects on the results. After the LRF computation we sample  $n = 512$  points per patch to train our deep network. The descriptor dimension is always set to  $d = 32$  as in recent state-of-the-art approaches [7], [8], [10], [16], [17]. We set  $r = .5m$  for 3DMatch and  $r = 2.5m$  for KITTI. In 3DMatch we train for 10 epochs, performing 16K iterations per epoch. Each iteration is a point cloud pair. In KITTI we train for 122 epochs, performing 1.4K iterations per epoch. We use Stochastic Gradient Descent with an initial learning rate of  $10^{-1}$  that decreases by a factor .1 every 3 epochs in 3DMatch and every 35 epochs in KITTI. We use a weight decay equal to  $5 \cdot 10^{-5}$  and Dropout with probability .3 at the last MLP layer. As in [7], we set  $m_+ = .1$  and  $m_- = 1.4$  (Eq. 8). We set  $r_c = .2r$ . We apply data augmentation on the canonicalised patches to simulate noisy LRF computations. Specifically, we apply a random 3D rotation by independently sampling the three angles within the interval  $[-10^\circ, 10^\circ]$ .

For testing, we set  $n = 1024$  as we found it works well in practice. The radius of the patches are set to  $r = .6m$  in 3DMatch,  $r = 1.5m$  in ETH and  $r = 2.5m$  in KITTI. Sec. 4.7 reports our ablation study on the behaviour of different values of  $n$  and  $r$ . As for the other approaches, in 3DMatch and ETH, we compute the descriptors for 5K randomly sampled points from each point cloud and compute their FMR scores. This number of points produces about 8.1M and 3.6M descriptors that are being tested for 3DMatch and ETH, respectively. Unlike 3DMatch and ETH, KITTI is typically tested by computing the descriptor of each point and by estimating the rigid transformation between two point clouds through RANSAC [10]. Because each point cloud of KITTI includes 120K+ points, the computation of a descriptor for each point is a rather lengthy process. Therefore, we run the experiments using 25K and 50K randomly sampled points from each point cloud, and compare our results against those of the other approaches in their original setup. Note that our setup is more challenging than theirs as it requires a greater discriminative ability of the descriptors as fewer are used.

## 4.4 RGBD indoors → laser scanner outdoors

Tab. 1 shows the results of GeDi trained on 3DMatch and tested on ETH. GeDi outperforms the other approaches by a large margin, improving by 5.4% in terms of FMR with respect to DIP [9] and SpinNet [10]. Tab. 2 shows the results of GeDi trained on 3DMatch and tested on KITTI. Also on KITTI, GeDi outperforms by a large margin its competitors,

TABLE 1  
Feature-matching recall computed in the setting:  
3DMatch (training) → ETH (testing).

Method	Gazebo		Wood		avg ↑
	Summer	Winter	Autumn	Summer	
	Ξ ↑	Ξ ↑	Ξ ↑	Ξ ↑	
FPFH [4]	.386	.142	.148	.208	.221
SHOT [15]	.739	.457	.609	.640	.611
3DMatch [5]	.228	.083	.139	.224	.169
CGF [45]	.375	.138	.104	.192	.202
PerfectMatch [16]	.913	.841	.678	.728	.790
FCGF [7]	.228	.100	.148	.168	.161
D3Feat-rand [8]	.457	.239	.130	.224	.262
D3Feat-pred [8]	.859	.630	.496	.480	.563
LMVD [17]	.853	.630	.496	.480	.616
DIP [9]	.908	.886	.965	.952	.928
SpinNet [10]	.929	.917	.922	.944	.928
GeDi	<b>.989</b>	<b>.965</b>	<b>.974</b>	<b>1.000</b>	<b>.982</b>

achieving a success rate of +5.23% with respect to DIP [9] and +16.76% with respect to SpinNet [10].

These experiments show us that deep learning-based two-stage descriptors (i.e. PerfectMatch, LMVD, DIP, SpinNet, GeDi) are the best performing ones as they work on local information. Whereas deep learning-based one-stage descriptors, i.e. FCGF and D3Feat, which use fully convolutional deep networks, show weaker generalisation ability. On the one hand, we believe that processing whole point clouds may hinder descriptor generalisation as local geometric structures should in principle be more repeatable across different contexts/datasets. For example, a corner of an indoor surface is likely to have a more similar geometric structure to a corner of an outdoor surface, whereas the geometric structure of a kitchen is likely to be dissimilar to the structure of a road. On the other hand, PerfectMatch, LMVD and SpinNet use projection layers to build suitable representations, e.g. cylindrical [10] or multi-view projections [17], which are then processed by traditional 2D or 3D convolutional deep networks. Although different projection strategies have been proposed to preserve most of the original 3D information and to enable invariance to different geometric transformations, we can experimentally observe that they still appear to have inferior generalisation ability compared to architectures that consume 3D points directly, like DIP and GeDi. This behaviour is particularly visible in the case of KITTI where DIP and GeDi largely outperform SpinNet. Both DIP and GeDi purposely produce descriptors using normalised patches in order to be scale invariant. To further improve the intra-patch geometric structure representation, we exploit the design of PointNet++ that uses cascades of receptive fields with different sizes to build hierarchical local geometric representations at different scales, allowing us to effectively capture and aggregate local geometric contexts. From the experiments we can observe that this design have a positive effect on the generalisation ability of GeDi compared to DIP, which instead uses a single receptive field.

#### 4.5 Laser scanner outdoors → RGBD indoors

Tab. 3 confirms the generalisation ability of GeDi across different sensors and contexts, i.e. when the deep network

TABLE 2  
Relative Translational Error (RTE) and Relative Rotation Error (RRE)  
computed in the setting: 3DMatch (training) → KITTI (testing).

Method	RTE(cm)		RRE(°)		Succ.(%)↑
	avg ↓	std ↓	avg ↓	std ↓	
FCGF [7]	27.10	5.58	1.61	1.51	24.19
D3Feat-rand [8]	37.80	9.98	1.58	1.47	18.47
D3Feat-pred [8]	31.60	10.10	1.44	1.35	36.76
SpinNet [10]	15.60	1.89	.98	.63	81.44
DIP [9]	9.12	.76	.56	.69	92.97
GeDi	<b>8.23</b>	<b>.66</b>	<b>0.38</b>	<b>.46</b>	<b>98.20</b>

TABLE 3  
Feature-matching recall computed in the setting:  
KITTI (training) → 3DMatch (testing).

Method	3DMatch		3DMatchRotated	
	Ξ ↑	std ↓	Ξ ↑	std ↓
FPFH [4]	.359	.134	.364	.136
SHOT [15]	.238	.109	.234	.095
FCGF [7]	.325	.074	.010	.010
D3Feat-rand [8]	.607	.077	.172	.046
D3Feat-pred [8]	.627	.081	.178	.032
SpinNet [10]	.845	<b>.059</b>	.842	<b>.058</b>
GeDi	<b>.922</b>	<b>.059</b>	<b>.919</b>	.059

model is trained on KITTI and tested on 3DMatch. A similar behaviour to that we described in Sec. 4.4 can also be observed in this experiment. FCGF and D3Feat show lower generalisation ability than SpinNet and GeDi, and, importantly, a significant drop in performance when tested on 3DMatchRotated, suggesting that their model cannot effectively learn general rotation invariant and repeatable geometric representations. Although FPFH and SHOT are the worst performing ones on 3DMatch, we can observe that their performance is consistent, and better than FCGF and D3Feat, on 3DMatchRotated. GeDi outperforms SpinNet by 7.7% both on the original and on the augmented version of 3DMatch, suggesting that GeDi’s design to produce descriptors from raw 3D points promotes generalisation. Graphical representations of these results can be found in the project page<sup>4</sup>.

#### 4.6 Same settings

Tab. 4 reports the results of GeDi on 3DMatch, using its original train/test split. Although the splits ensure that point clouds of the test set are not used for training, the point clouds of both sets were captured with similar sensors in similar contexts. GeDi outperforms all the competitor descriptors on both 3DMatch and 3DMatchRotated, thus showing its great distinctiveness ability also on data of the same domain. Fig. 4 provides a more detailed picture of the results on 3DMatch by varying  $\tau_2$  and  $\tau_1$  of Eq. 10, which are the inlier ratio and distance thresholds, respectively. We can observe that GeDi can produce a larger number of distinctive descriptors than SpinNet, especially when the inlier threshold is set to .20, where the feature-matching recall improvement is 4.8%.

4. <https://github.com/fabiopoesi/gedi>.

TABLE 4  
Feature-matching recall computed in the setting:  
3DMatch (training) → 3DMatch (testing).

Method	3DMatch		3DMatchRotated		Feat. dim. ↓
	Ξ ↑	std ↓	Ξ ↑	std ↓	
Spin [14]	.227	.114	.227	.121	153
SHOT [15]	.238	.109	.234	.095	352
FPFH [4]	.359	.134	.364	.136	33
USC [15]	.400	.125	-	-	1980
CGF [45]	.582	.142	.585	.140	32
3DMatch [5]	.596	.088	.011	.012	512
Folding [46]	.613	.087	.023	.010	512
PPFNet [6]	.623	.108	.003	.005	64
PPF-FoldNet [18]	.718	.105	.731	.104	512
DirectReg [19]	.746	.094	-	-	512
CapsuleNet [20]	.807	.062	.807	.062	512
PerfectMatch [16]	.947	.027	.949	.024	32
DIP [9]	.948	.046	.946	.046	32
FCGF [7]	.952	.029	.953	.033	32
D3Feat-rand [8]	.953	.027	.952	.032	32
D3Feat-pred [8]	.958	.029	.955	.035	32
LMVD [17]	.975	.028	.969	-	32
SpinNet [10]	.976	<b>.019</b>	.975	<b>.019</b>	32
GeDi	<b>.979</b>	.022	<b>.976</b>	.027	32

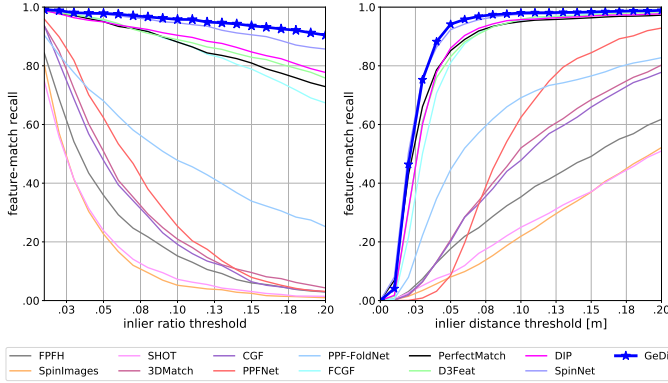


Fig. 4. Feature-matching recall as a function of (left)  $\tau_2$  and (right)  $\tau_1$ .

Tab. 5 reports the results of GeDi on KITTI, using its original train/test split. GeDi achieves a success rate of 99.82%, which means that only one pair out of 555 failed the geometric registration. The success rate of GeDi is similar to that of D3Feat, which is based on a fully convolutional deep network. On average, D3Feat-pred’s RTE and RRE are .65cm and 9° lower than GeDi, respectively. We attribute this difference and the relative lower standard deviation to the voxelisation preprocessing that D3Feat performs on the input point cloud, thus leading to a slightly more accurate estimated geometric transformation. In our case, we do not apply any preprocessing to the point clouds as it makes them sparser, thus affecting the density of the support used by GeDi to compute the local reference frames and the descriptors. Although the translational and rotational errors are lower in the case of D3Feat, we deem GeDi’s result comparable to that of D3Feat-pred as the transformation is estimated by an external algorithm that can be improved, for example, by refining the result through

TABLE 5  
Relative Translational Error (RTE) and Relative Rotation Error (RRE)  
computed in the setting: KITTI (training) → KITTI (testing).

Method	RTE(cm)		RRE(°)		Succ.(%)↑
	avg ↓	std ↓	avg ↓	std ↓	
3DFeat-Net [42]	25.9	26.2	.57	.46	95.97
FCGF [7]	9.52	1.30	.30	.28	96.57
DIP (25K points) [9]	8.69	.69	.44	.49	97.30
SpinNet [10]	9.88	.50	.47	.09	99.10
D3Feat-rand [8]	8.78	.44	.32	.07	99.81
D3Feat-pred [8]	<b>6.90</b>	<b>.30</b>	<b>.24</b>	<b>.06</b>	99.81
GeDi (25K points)	7.22	.63	.32	.27	99.46
GeDi (50K points)	7.55	.67	.33	.31	<b>99.82</b>

TABLE 6  
Ablation study using the feature-matching recall as a function of the  
number of sampled points on the 3DMatch dataset [5].

Method	# sampled points					avg ↑
	5000	2500	1000	500	250	
PerfectMatch [16]	.947	.942	.926	.901	.829	.909
FCGF [7]	.952	.955	.946	.930	.899	.936
D3Feat-rand [8]	.953	.951	.942	.936	.908	.938
D3Feat-pred [8]	.958	.956	.946	.943	.933	.947
SpinNet [10]	.976	.975	.973	.963	.943	.966
GeDi	<b>.979</b>	<b>.977</b>	<b>.976</b>	<b>.972</b>	<b>.973</b>	<b>.975</b>

ICP. Moreover, D3Feat-pred uses a keypoint detector to predict which points are the most likely ones that provide highly informative and distinctive descriptors. In our case, as well as in FCGF, DIP, SpinNet and D3Feat-rand, there is no keypoint selection. Instead, the selection of the points is performed randomly in these cases. Under this setup, we can observe that GeDi outperforms all the other methods, even using a subset of the point cloud points.

#### 4.7 Ablation study

We investigate the distinctiveness ability of GeDi by reducing the number of sampled points in the 3DMatch dataset [10]. Tab. 6 reports and compares GeDi’s FMR scores to those of the other descriptors when the number of sampled points is reduced from 5000 to 250. We can observe that GeDi maintains a high level of distinctiveness, even when as little as 250 points are sampled. Based on the formulation of FMR (Eq. 10), this experiment shows us that if we randomly pick 250 points, 97.3% of them on average are mutual nearest neighbour descriptors of corresponding points. Therefore, the likelihood that RANSAC will successfully register two point clouds of this test set is rather high. GeDi outperforms the most recent local deep descriptor SpinNet by .9% on average, especially by 3% on the experiment where 250 points are sampled. Interestingly, we also outperform by 2.8% on average the result of D3Feat-pred, albeit its dedicated module to detect reliable keypoints.

We analyse the key implementation settings of GeDi by ablating different modules. We use a subset of 3DMatch’s training set, and define our own training and validation sets. We use *7-scenes-chess* and *7-scenes-fire* for training, and *7-scenes-office* and *7-scenes-pumpkin* for validation. The number

of point cloud pairs are 2492 for training and 1640 for validation. In validation, we randomly sample 5K points for each point cloud pair, resulting in 8.2M descriptor evaluated in this ablation study. We train with the same parameters described in Sec. 4.3.

The first part of Tab. 7 reports the ablation study that assesses the choice of QNet vs. TNet, and the importance of LRF to canonicalise the input patches before passing them to the deep network. We observed that TNet is unsuitable for a deep network with fixed receptive fields as the transformation produced by TNet scales and skews the input 3D points, thus leading to unstable internal representations. TNet can be a valid solution if used along with PointNet-like architectures where there is no concept of hierarchical receptive fields. Unlike TNet, we can see in the last row of this table that our QNet is effective and allows the network to correctly learn the internal representations through the receptive field hierarchy. We can observe that QNet provides better results than the version without it, suggesting that QNet can learn to correct eventual noisy rotations that the local reference frame algorithm estimates due to clutter or occlusions. Then, we can also see that LRF is key to achieve descriptor rotation invariance as the performance drop close to zero in the case of 3DMatchRotated.

The second part of Tab. 7 reports the ablation study that assesses the descriptors’ output dimension. We trained and evaluated GeDi with dimensions equal to 16, 32, 64 and 128. We can observe an improvement in the FMR score as the dimension increases, suggesting that the more the capacity to encode the information in descriptors of larger dimension, the better the performance. In the comparative analysis we reported in the previous sections, we used 32-dimensional descriptors for fairness to the other approaches.

The third part of Tab. 7 reports the ablation study that assesses the number of points sampled from each patch before passing them to the deep network. We can observe an improvement in the FMR score as the number of points increases. Although the deep network is trained using 512 points as input, we can see that it can effectively handle a larger number of input points. However, we experimentally experienced a higher processing time when a larger number of input points is used. This motivates our choice of using  $n = 1024$  throughout our experiments in order to have feedback in reasonable amounts of time.

Lastly, the fourth part of Tab. 7 reports the ablation study that assesses the size of the patch radius. On the one hand, when the radius is too small, the captured geometric information is not sufficient to achieve an adequate level of distinctiveness. On the other hand, when the radius is too large, a larger amount of contextual information is encoded, thus affecting distinctiveness. To quantitatively assess this behaviour, we monitored the distinctiveness level throughout training by comparing the cases when descriptors are learned using patch radii equal to .5 and 3.0. We computed the Euclidean distance between a chosen descriptor and all the other descriptors of the point cloud, and colour-coded this distance with respect to all points on the point cloud. Fig. 5 shows the colour-coded point clouds for the descriptor distances computed with radius .5 (top) and with radius 3.0 (bottom). The top row of the figure shows a rather localised region of low distances, i.e. only few descriptors

TABLE 7  
 Ablation study on GeDi’s implementation settings.  
 Key: ST: Spatial Transformer network. LRF: Local Reference Frame.  
 The last row is our setting in all the other experiments.

$d$	$n$	$r$	ST	LRF	3DMatch			3DMatchRotated		
					$\Xi \uparrow$	$\mu_{\xi} \uparrow$	$\sigma_{\xi} \downarrow$	$\Xi \uparrow$	$\mu_{\xi} \uparrow$	$\sigma_{\xi} \downarrow$
32	1024	.6		✓	.917	.254	.182	.919	.255	.182
32	1024	.6	tnet	✓		.....	loss diverged	.....		
32	1024	.6	qnet		.787	.206	.191	.019	.007	.018
16	1024	.6	qnet	✓	.902	.222	.164	.905	.224	.164
64	1024	.6	qnet	✓	.937	.268	.186	.934	.269	.186
128	1024	.6	qnet	✓	.937	.277	.189	.942	.277	.190
32	256	.6	qnet	✓	.903	.206	.146	.896	.207	.146
32	512	.6	qnet	✓	.928	.252	.176	.926	.253	.176
32	1536	.6	qnet	✓	.934	.269	.187	.934	.268	.187
32	2048	.6	qnet	✓	.937	.269	.187	.935	.269	.187
32	1024	.2	qnet	✓	.741	.128	.112	.741	.128	.113
32	1024	1.0	qnet	✓	.766	.178	.166	.763	.179	.167
32	1024	1.4	qnet	✓	.510	.100	.121	.506	.101	.122
32	1024	1.8	qnet	✓	.315	.059	.084	.306	.058	.085
32	1024	.6	qnet	✓	.932	.267	.185	.931	.268	.186

in the neighbourhood of the chosen descriptor have a low distance. Differently, the bottom row of the figure shows that a larger amount of contextual information encoded in the descriptor affects distinctiveness. The radius of the patch also affects the training time, in fact we can see that the case on the top row can achieve a better distinctiveness with fewer training iterations than case on the bottom row, i.e. an average distance of .942 is reached in 1500 iterations when the patch radius is .5, while the same distance is reached at iteration 5980 when the patch radius is 3.0.

#### 4.8 Qualitative results

Fig. 6 shows a selection of qualitative registration results computed on ETH, KITTI and 3DMatch datasets using the GeDi descriptors trained on 3DMatch. The registration is performed using RANSAC [12], [43]. These results show the context and sensor diversity that GeDi can effectively handle. Although ETH and KITTI are datasets collected outdoors and with laser scanners, we can see that the structure of the environment is rather different between themselves. ETH mainly includes natural elements, such as vegetation, whereas KITTI mainly includes man-made structures, such as cars and roads. Figs. 6a-g are correct registration results where we highlighted some elements to facilitate the analysis of the results. In (a-c) we can see that the results are correct by looking at the overlapping 3D points on the leaves or on the trees. Despite the absence of structures like those in (f,g,i) (modality used in training), we can see that GeDi descriptors successfully generalise to ETH scenes. In (d,e) we can see correct registration results on KITTI, whereas in (h) we included the point cloud pair that was incorrectly registered in the quantitative evaluation described in Sec. 4.6. This pair is indeed rather challenging because the overlap region between the two point clouds contains partial structures with little geometric information. In (f,g) we can see correct registration results on 3DMatch: (f) is a case with small overlap where we can notice that

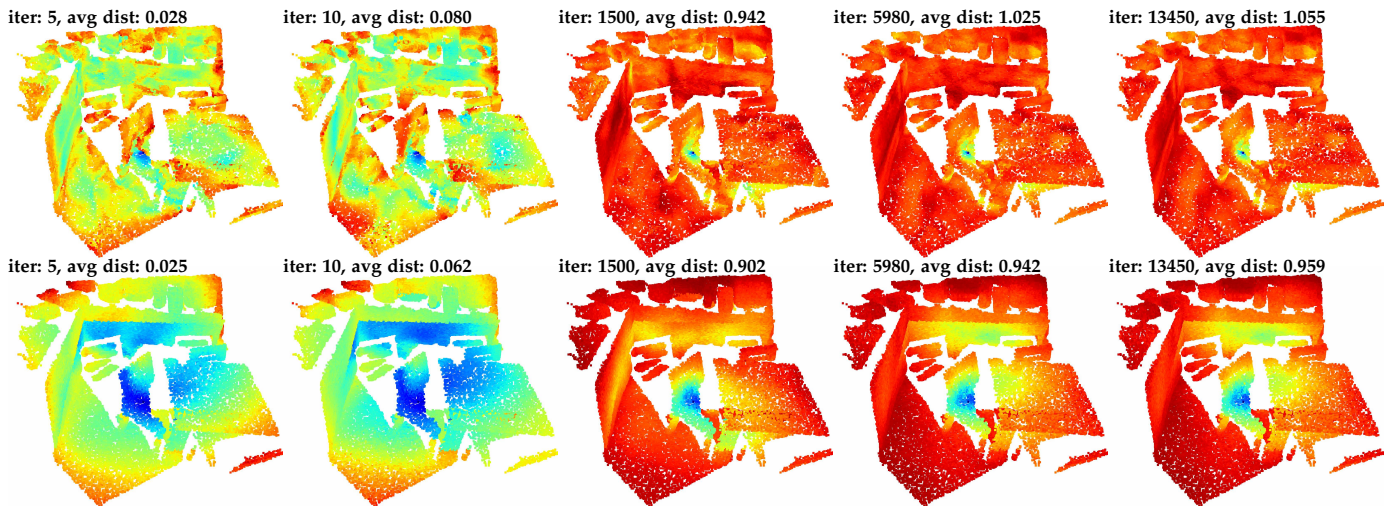


Fig. 5. Colour-coded point clouds illustrating the distance between a descriptor and all the other descriptors for each point. Red indicates large distance, while blue indicates small distance. We show the variation of the distance for a descriptor trained using radius .5 (top) and using radius 3.0 (bottom). The chosen descriptor is from a point located on the chair’s seat in the centre of the image. Each figure reports the training iteration (iter) and the average distance computed with respect to all the descriptors. The top row shows that only few descriptors in the neighbourhood of the chosen descriptor have a low distance. The bottom row shows that a descriptors trained with a patch with large radius lacks distinctiveness.

the registration is correct but not highly accurate. This is due to the maximum correspondence point-pair distance of RANSAC that it is typically kept slightly loose in order to be robust against noise. A refinement with ICP would improve the registration; (g) is a case that contains both informative geometric structures (e.g. chairs, frames) and flat surfaces. This is a typical case where even if there are flat surfaces but also some objects in the overlap region, the descriptors sampled on the objects are those contributing to the correct registration. Unlike (g), in (i) we can notice that if there are flat surfaces and partially captured objects in the overlap region, the registration is more likely to fail.

## 5 CONCLUSIONS

We presented a novel approach to train local, compact, generalisable and distinctive 3D descriptors through a point permutation-invariant deep neural network using canonicalised patches. The quaternion transformation module embedded in our deep network improves patch canonicalisation and is trained concurrently with the encoding module. Distinctiveness is achieved by training our deep network with a Siamese approach using the hardest-contrastive loss that mines negatives outside a spherical region centred on each anchor. Compared with existing deep learning-based 3D descriptors, GeDi descriptors have the unique ability of being highly effective in generalisation across contexts and sensors, while also being as effective as the other descriptors when trained and tested in the same scenarios. Future research directions include building end-to-end trainable descriptors and designing a strategy to learn patch radii.

## REFERENCES

- [1] T. Truong, M. Yamaguchi, S. Mori, V. Nozick, and H. Saito, “Registration of RGB and thermal point clouds generated by structure from motion,” in *Proc. of IEEE ICCV*, Venice, IT, Oct 2017.
- [2] J. Du, R. Wang, and D. Cremers, “DH3D: Deep Hierarchical 3D Descriptors for Robust Large-Scale 6DoF Relocalization,” in *Proc. of ECCV*, Virtual, Aug 2020.
- [3] B. Drost, M. Ulrich, N. Navab, and S. Ilic, “Model Globally, Match Locally: Efficient and Robust 3D Object Recognition,” in *Proc. of IEEE CVPR*, San Francisco, US, Jun 2010.
- [4] R. Rusu, N. Blodow, and M. Beetz, “Fast point feature histograms for 3D registration,” in *Proc. of IEEE ICRA*, Kobe, JP, May 2009.
- [5] A. Zeng, S. Song, M. Niessner, M. Fisher, J. Xiao, and T. Funkhouser, “3DMatch: Learning the matching of local 3D geometry in range scans,” in *Proc. of IEEE CVPR*, Hawaii, US, Jul 2017.
- [6] H. Deng, T. Birdal, and S. Ilic, “PPFNet: Global context aware local features for robust 3D point matching,” in *Proc. of IEEE CVPR*, Salt Lake City, US, Jun 2018.
- [7] C. Choy, J. Park, and V. Koltun, “Fully Convolutional Geometric Features,” in *Proc. of IEEE ICCV*, Seoul, KR, Oct 2019.
- [8] X. Bai, Z. Luo, L. Zhou, H. Fu, L. Quan, and C.-L. Tai, “D3Feat: Joint Learning of Dense Detection and Description of 3D Local Features,” in *Proc. of IEEE CVPR*, Virtual, Jun 2020.
- [9] F. Poiesi and D. Boscaini, “Distinctive 3D local deep descriptors,” in *Proc. of IEEE ICPR*, Virtual, Jan 2021.
- [10] S. Ao, Q. Hu, B. Yang, A. Markham, and Y. Guo, “SpinNet: Learning a General Surface Descriptor for 3D Point Cloud Registration,” in *Proc. of IEEE CVPR*, Virtual, Jun 2021.
- [11] P. Besl and N. McKay, “A method for registration of 3-d shapes,” *IEEE Trans. on PAMI*, vol. 14, no. 2, pp. 239–256, Feb 1992.
- [12] M. Fischler and R. Bolles, “Random sample consensus: A paradigm for model fitting with applications to image analysis and automated cartography,” *Commun. ACM*, vol. 24, no. 6, pp. 341–406, Jun 1981.
- [13] A. Geiger, P. Lenz, and R. Urtasun, “Are we ready for autonomous driving? The KITTI vision benchmark suite,” in *Proc. of IEEE CVPR*, Providence, US, Jun 2012.
- [14] A. Johnson and M. Hebert, “Using spin images for efficient object recognition in cluttered 3D scenes,” *IEEE Trans. on PAMI*, vol. 21, no. 5, pp. 433–449, May 1999.
- [15] S. Salti, F. Tombari, and L. Di Stefano, “SHOT: Unique signatures of histograms for surface and texture description,” *CVIU*, vol. 125, pp. 251–264, Aug 2014.
- [16] Z. Gojcic, C. Zhou, J. Wegner, and W. Andreas, “The perfect match: 3D point cloud matching with smoothed densities,” in *Proc. of IEEE CVPR*, Long Beach, US, Jun 2019.
- [17] L. Li, S. Zhu, H. Fu, P. Tan, and C.-L. Tai, “End-to-End Learning Local Multi-view Descriptors for 3D Point Clouds,” in *Proc. of IEEE CVPR*, Virtual, Jun 2020.
- [18] H. Deng, T. Birdal, and S. Ilic, “PPF-FoldNet: Unsupervised learning of rotation invariant 3D local descriptors,” in *Proc. of ECCV*, Munich, GE, Sep 2018.
- [19] —, “3D local features for direct pairwise registration,” in *Proc. of IEEE CVPR*, Long Beach, US, Jun 2019.

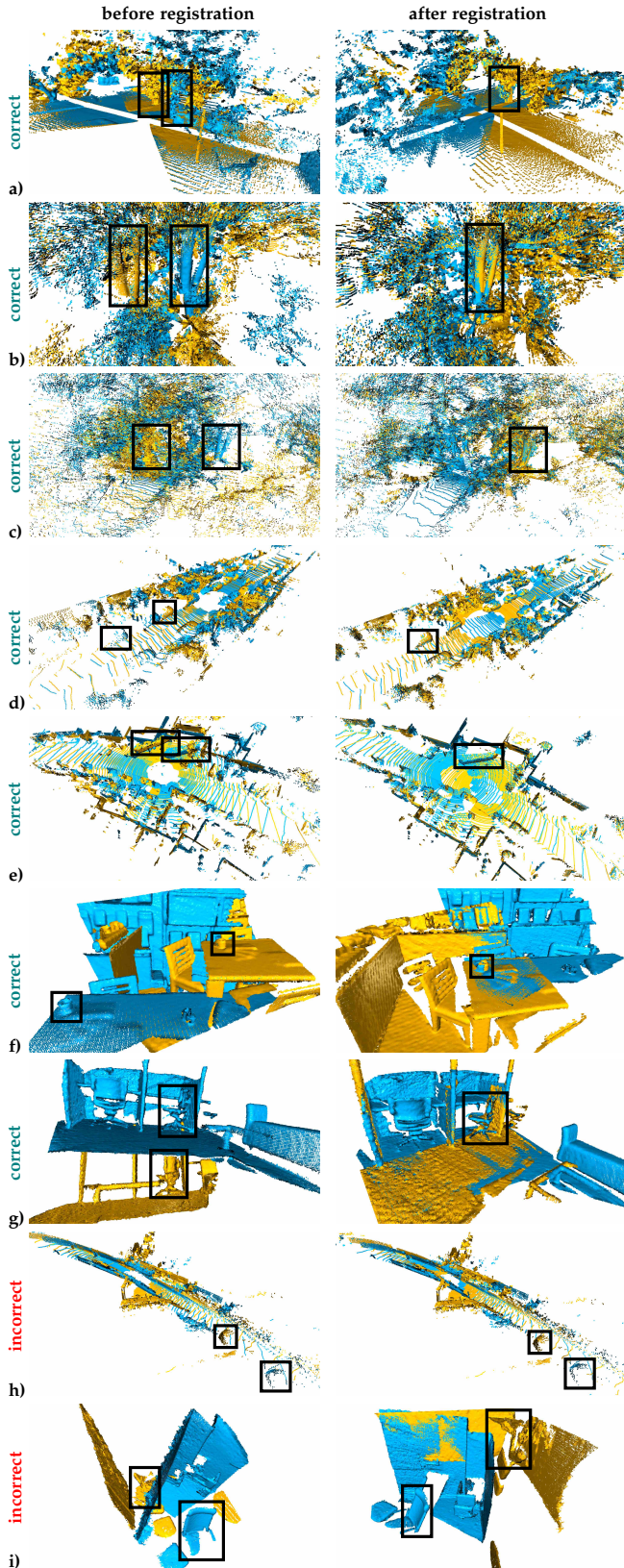


Fig. 6. Qualitative registration results computed on (a-c) ETH, (d,e,h) KITTI and (f,g,i) 3DMatch datasets using the GeDi descriptors trained on 3DMatch. The point clouds are in their original reference frame *before registration* (left-hand side column) and in a common reference frame *after registration* (right-hand side column). We included *correct* and *incorrect* registration results. We highlighted some regions of interest to facilitate the analysis of the results.

[20] Y. Zhao, T. Birdal, H. Deng, and F. Tombari, "3D point capsule networks," in *Proc. of IEEE CVPR*, Long Beach, US, Jun 2019.

[21] Y. Zhong, "Intrinsic shape signatures: A shape descriptor for 3D object recognition," in *Proc. of IEEE ICCV*, Kyoto, JP, Sep 2009.

[22] J. Yang, Q. Zhang, Y. Xiao, and Z.-G. Cao, "TOLDI: An effective and robust approach for 3D local shape description," *Pattern Recognition*, vol. 65, pp. 175–187, May 2017.

[23] C. Qi, L. Yi, H. Su, and L. Guibas, "PointNet++: Deep Hierarchical Feature Learning on Point Sets in a Metric Space," in *Proc. of NIPS*, Long Beach, US, Dec 2017.

[24] F. Pomerleau, M. Liu, F. Colas, and R. Siegwart, "Challenging data sets for point cloud registration algorithms," *IJRR*, vol. 31, no. 14, pp. 1705–1711, Dec 2012.

[25] Q. Hu, B. Yang, L. Xie, S. Rosa, Y. Guo, Z. Wang, N. Trigoni, and A. Markham, "RandLA-Net: Efficient Semantic Segmentation of Large-Scale Point Clouds," in *Proc. of IEEE CVPR*, Virtual, Jun 2020.

[26] Q.-Y. Zhou, J. Park, and V. Koltun, "Fast global registration," in *Proc. of ECCV*, Amsterdam, NL, Oct 2016.

[27] P. Cirujeda, X. Mateo, Y. Cid, and X. Binefa, "MCOV: a covariance descriptor for fusion of texture and shape features in 3D point clouds," in *Proc. of 3DV*, Tokyo, JP, Dec 2014.

[28] Y. Guo, F. Sohel, M. Bennamoun, M. Lu, and J. Wan, "Rotational projection statistics for 3D local surface description and object recognition," *IJCV*, vol. 105, pp. 63–86, Apr 2013.

[29] C. Qi, H. Su, K. Mo, and L. Guibas, "PointNet: Deep learning on point sets for 3D classification and segmentation," in *Proc. of IEEE CVPR*, Hawaii, US, Jul 2017.

[30] Y. Yang, C. F. Y. Shen, and D. Tian, "FoldingNet: Point cloud auto-encoder via deep grid deformation," in *Proc. of IEEE CVPR*, Salt Lake City, US, Jun 2018.

[31] C. Choy, J. Gwak, and S. Savarese, "4D Spatio-Temporal ConvNets: Minkowski Convolutional Neural Networks," in *Proc. of IEEE CVPR*, Long Beach, US, Jun 2019.

[32] H. Thomas, C. Qi, J.-E. Deschaud, B. Marcotegui, F. Goulette, and L. Guibas, "KPConv: Flexible and deformable convolution for point clouds," in *Proc. of IEEE ICCV*, Venice, IT, Oct 2017.

[33] Y. Wang, Y. Sun, Z. Liu, S. Sarma, M. Bronstein, and J. Solomon, "Dynamic Graph CNN for Learning on Point Clouds," *ACM Transactions on Graphics*, vol. 38, no. 5, pp. 1–17, Oct 2019.

[34] Y. Tian, B. Fan, and F. Wu, "L2-Net: deep learning of discriminative patch descriptor in Euclidean space," in *Proc. of IEEE CVPR*, Hawaii, US, Jul 2017.

[35] W. Yuan, D. Held, C. Mertz, and M. Hebert, "Iterative Transformer Network for 3D Point Cloud," in *arXiv:1811.11209*, 2018.

[36] H. Abdi and L. Williams, "Principal Component Analysis," *Computational Statistics*, vol. 2, no. 4, pp. 433–459, Aug 2010.

[37] J. Valentin, A. Dai, M. Nießner, P. Kohli, P. Torr, S. Izadi, and C. Keskin, "Learning to navigate the energy landscape," in *Proc. of 3DV*, Stanford, US, Dec 2016.

[38] J. Shotton, B. Glocker, C. Zach, S. Izadi, A. Criminisi, and A. Fitzgibbon, "Scene coordinate regression forests for camera relocalization in RGB-D images," in *Proc. of IEEE CVPR*, Portland, US, Jun 2013.

[39] J. Xiao, A. Owens, and A. Torralba, "SUN3D: A Database of Big Spaces Reconstructed using SfM and Object Labels," in *Proc. of IEEE ICCV*, Sydney, AU, Apr 2013.

[40] V. G. Kim, S. Chaudhuri, L. Guibas, and T. Funkhouser, "Shape2Pose: human-centric shape analysis," *TOG*, vol. 33, no. 4, pp. 1557–7368, Jul 2014.

[41] M. Halber and T. Funkhouser, "Structured global registration of RGB-D scans in indoor environments," *arXiv:1607.08539*, 2016.

[42] Z. Yew and G. Lee, "3DFeat-Net: Weakly supervised local 3D features for point cloud registration," in *Proc. of ECCV*, Munich, GE, Sep 2018.

[43] Q.-Y. Zhou, J. Park, and V. Koltun, "Open3D: A modern library for 3D data processing," *arXiv:1801.09847*, 2018.

[44] Y. Ma, Y. Guo, J. Zhao, M. Lu, J. Zhang, and J. Wan, "Fast and accurate registration of structured point clouds with small overlaps," in *Proc. of IEEE CVPR Workshops*, Las Vegas, US, Jun 2016.

[45] M. Khoury, Q.-Y. Zhou, and V. Koltun, "Learning compact geometric features," in *Proc. of IEEE ICCV*, Venice, IT, Oct 2017.

[46] Y. Yang, C. Feng, Y. Shen, and D. Tian, "FoldingNet: Interpretable unsupervised learning on 3D point," in *Proc. of IEEE CVPR*, Hawaii, US, Jul 2017.

PLACE  
PHOTO  
HERE

**Fabio Poiesi** is a Researcher Scientist in the Technologies of Vision Lab at Fondazione Bruno Kessler in Trento, Italy. He received his Ph.D. degree in Electronic Engineering and Computer Science from Queen Mary University of London (UK) in March 2014. He spent nearly three years as a Postdoctoral Research Assistant in Queen Mary University of London. He participated in several European Projects, e.g. H2020 REPLICATE, EIT UAV-Retina, H2020 MiMEX, and he is now Principal Investigator in JPI-CH SHIELD.

He served as Area Chair in IEEE ICPR 2020 and appeared in the honourable mentions of outstanding reviewers in BMVC 2019. His research interests are 3D scene understanding, object detection and tracking, and extended reality.

PLACE  
PHOTO  
HERE

**Davide Boscaini** is a Researcher Scientist in the Technologies of Vision Lab at Fondazione Bruno Kessler in Trento, Italy. He received his Ph.D. degree in Computational Science from Università della Svizzera Italiana (USI) in Lugano (CH) in August 2017. His main research interests are in the fields of 3D Computer Vision and 3D Deep Learning. He is one of the pioneers of Geometric Deep Learning. His work was featured on the cover of Nature Methods in February 2020. He is the inventor of two US

patents on these topics that were later acquired by Twitter Inc. in 2020.